Bulletin of Engineering Geology and the Environment (2023) 82:435
https://doi.org/10.1007/s10064-023-03452-5

ORIGINAL PAPER

An experimental investigation on the failure behaviour of surrounding rock in the stress concentration area of deeply buried tunnels

Lei Shi[1,2] · Xiwei Zhang[1,2]

Received: 13 May 2023 / Accepted: 16 October 2023 / Published online: 6 November 2023

Abstract

To investigate the failure behaviour of the stress concentration areas of deeply buried hard rock tunnels, model tests under uniaxial and biaxial loading conditions and a single-free-face true triaxial compression (TTC) test were carried out on Beishan granite. The failure forms of the specimens under the above three loading conditions are different: under the first loading condition, the model specimen was prone to tensile fracturing at the tensile stress concentration the at top and bottom of the hole, which is similar to splitting along a road tunnel; under the second loading condition, the sidewall of the model specimen was progressively damaged and ultimately formed breakout notches, which is similar to spalling failure in deep engineering; under the third loading condition, the prismatic specimen underwent a slight strain burst. Since the failure of the specimen under the latter two loading conditions was induced by compressive stress concentrations, the reasons for the difference in the failure behaviours of the specimens in these two types of tests were discussed. It was found that the intrinsic potential energy (W_{bk}) of the rock determines the failure form of the specimen. For rock model tests with lateral stress, rock with a high W_{bk} fails by strain bursting, and rock with a low W_{bk} fails by spalling. However, for intact rock specimens under single-free-face TTC, a low W_{bk} can induce strain bursts. The outcome of this research could be applied to rock failure behaviour analysis around underground excavations in deep hard rock engineering.

Keywords Strain burst · Rock spalling · Hole breakout · Splitting · Strain energy

Introduction

The rock in deeply buried hard rock tunnels may fail by splitting, spalling, and rock burst throughout excavation, as shown in Fig. 1. The first failure type separates the rock perpendicular to the newly created fracture surfaces and is caused by a tensile or compressive stress applied perpendicular to the fracture plane. Spalling refers to a failure mode in which the rock fractures parallel to the sidewalls of the excavation under high tangential compressive stresses and the thin rock slabs peel off and fall (Fairhurst and Cook 1966). These two failure types are static failure behaviours, and they affect the stability of deeply buried tunnels. In a rock burst, rock is ejected or remarkably displaced. Based on the triggering mechanisms, there are two types of rock bursts: strain bursts associated with overstressing and fault-slip bursts associated with the slippage of preexisting faults (Wan and Li 2022). Strain bursts are caused by the conversion of excess energy into kinetic energy as the strain energy stored in the burst rock exceeds that consumed during its fracturing. Thus, strain bursting is a dynamic failure behaviour that not only affects the stability of deeply buried tunnels but also threatens the safety of construction personnel.

The main reason for the failure of deeply buried tunnels is the formation of tensile stress and compressive stress concentration areas in the surrounding rock mass induced by excavation. Before excavation, the rock is subjected to true triaxial stress with $\sigma_1 > \sigma_2 > \sigma_3$, where σ_1, σ_2, and σ_3 are the maximum, intermediate, and minimum principal stresses, respectively, as shown in Fig. 1c. After excavation, compressive stress concentration areas are formed in the sidewalls perpendicular to σ_1, and the stress state of an element at this position is changed to a state that is stressed on five of its six

✉ Xiwei Zhang
zhangxiwei@mail.neu.edu.cn

[1] Key Laboratory of Ministry of Education on Safe Mining of Deep Metal Mines, Northeastern University, Shenyang 110819, Liaoning, China

[2] Key Laboratory of Liaoning Province on Deep Engineering and Intelligent Technology, Northeastern University, Shenyang 110819, Liaoning, China

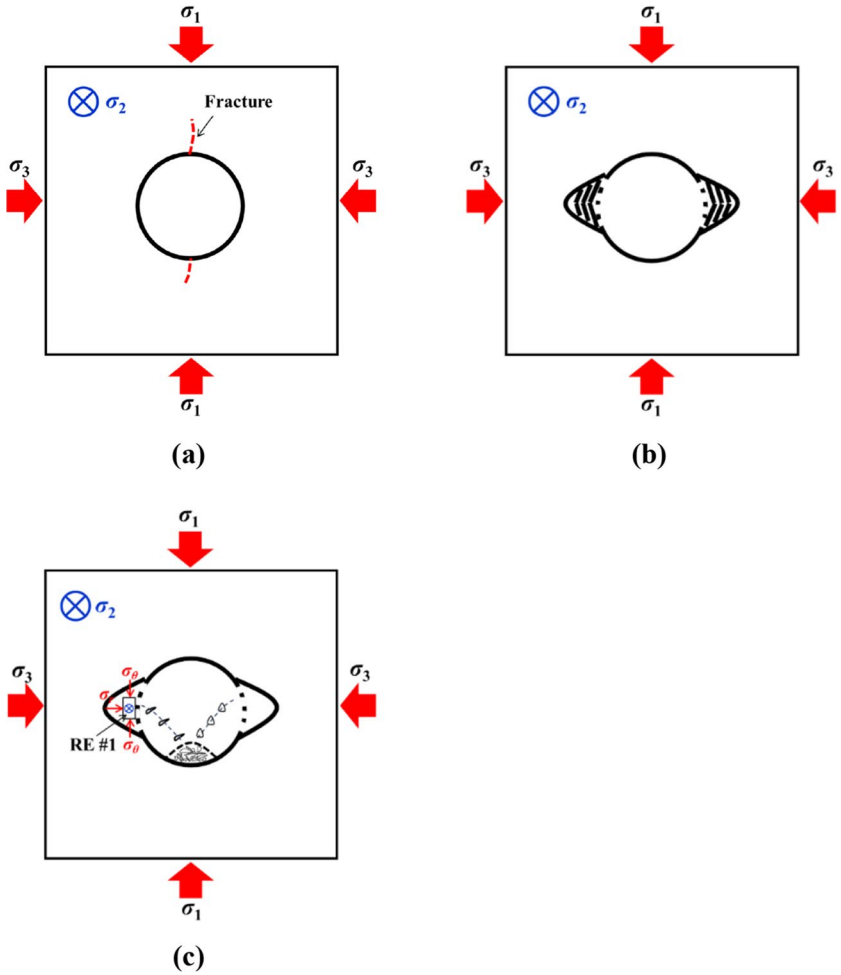

Fig. 1 Different failure forms in rock engineering: splitting (**a**), spalling (**b**), and rock bursting (**c**) (RE represents the rock element: σ_1, σ_2, and σ_3 are the maximum, intermediate, and minimum principal stresses, respectively; σ_r and σ_θ represent the radial stress and tangential stress, respectively)

faces, with one face stress-free, as shown in rock element #1 in Fig. 1c. The radial stress (σ_r) on the free surface is zero, but it is slightly greater than zero on the face of this rock element opposite to the free surface. The tangential stress (σ_θ) gradually increases during excavation. When σ_θ exceeds the bearing capacity of the rock element, the rock fails.

There are two main types of laboratory tests used to study the failure behaviour of deeply buried tunnels. The first is the model test, which mainly simulates the overall failure behaviour of a deeply buried tunnel by loading a specimen with a hole. Related research mainly includes four aspects: (a) the effect of the size of the hole on breakout onset stress (Carter 1992; Cheon et al. 2011; Martin 1997); (b) the effect of the shape of the hole, such as circular, square, elliptical, and saddle, on the failure behaviour of the surrounding rock (Haimson and Lee 2004; Gong et al. 2018; Luo et al. 2019; Wang et al. 2021; Zhu et al. 2022); (c) the effect of geological conditions, such as weak interlayers, joints, bedding planes, and fractures, on the failure intensity of the surrounding rock (Sagong et al. 2011; Zhong et al. 2018; Lin et al. 2020); and (d) laboratory simulations of strain bursts and spalling (e.g., Fakhimi et al. 2002; Ohta and Aydan 2010; He et al. 2012; Hu et al. 2019; Zhang et al. 2020; Gong et al. 2020; Zhao et al. 2020; Wang et al. 2021). Among them, the fourth item is the research focus in recent years. This is due to the increase in the frequency of spalling and strain bursts at deeply buried tunnel projects. For example, Kusui et al. (2016) carried out model tests using granite and sandstone, and the specimens failed in the form of a strain burst, with a rock block ejection velocity of 3–6 m/s. Gong et al. (2018, 2019, 2020) conducted model tests with circular, arched, and rectangular hole shapes, and the model specimens exhibited both spalling failure and strain burst failure. Si et al. (2020, 2022) used model tests to study the effects of loading rate and bedding angle on rock burst intensity. The other main type of laboratory test is to carry out loading and unloading tests on intact rock specimens. Initially, this type of test was used to mainly conduct loading and unloading tests on cylindrical specimens subjected to symmetric stress states (conventional triaxial stress) or prismatic specimens subjected to asymmetric stress states (true triaxial stress) to simulate the stress adjustment process of rock elements at different positions. The corresponding experimental results were mainly used to analyse the strength, deformation, and fracture characteristics of rocks and provide

data support for numerical calculations (e.g., Von Karman 1911; Cook 1963; Mogi 1967; Haimson and Chang 2000; Lu et al. 2021; Shi et al. 2022, 2023b). However, this type of test cannot simulate the dynamic failure behaviour of rock, such as strain bursting. Some novel true triaxial rock burst test devices have been developed, and some strain burst simulation methods have been proposed, such as the "single-face or multiple-faces sudden unloading test", "single-free-face or multiple-free-faces true triaxial compression (TTC) test", and "single-face sudden unloading coupled dynamic disturbance test" (He et al. 2012, 2021; Li et al. 2015; Su et al. 2017a; Jiang et al. 2019). In such tests, the tested specimen is prismatic in shape and considered a burst body to simulate the stress adjustment process of a rock element on the sidewall of a tunnel structure, and a high-speed camera is used to capture the development process of the strain burst. Related research involves the influence of loading path, loading rate, dynamic disturbance parameters, and size effects on rock burst intensity (e.g., Zhao and Cai 2014; He et al. 2015; Du et al. 2016; Su et al. 2017a, 2017b, 2018).

The model test and the single-free-face TTC test are both effective means to study the failure behaviour of surrounding rocks in the stress concentration area. Among them, the former considers the structural effect of deeply buried tunnels, and the latter focuses on the stress adjustment process of representative rock elements. Although the specimen specifications of the above two test methods are different, the failure of the specimen is induced by stress concentration. In previous studies, these two types of tests have been carried out independently, and no case study has provided a comprehensive consideration of both. The differences and connections between the static or dynamic failure of the same material under the two loading modes are still unclear. In addition, what is the effect of lateral stresses on the failure of the model specimens? What are the characteristics of the strain energy in the surrounding rock induced by the hole and stress concentration? Notably, some rocks in previous model tests failed by spalling, and some failed by strain bursting; thus, the triggering condition of strain bursts is also worth analysing.

In response to the above questions, model tests under both uniaxial and biaxial loading conditions were first performed on Beishan granite. During the model tests, the surface strain of the specimens and the failure process of the hole were captured by the digital image correlation (DIC) technique and a video camera, respectively. Then, a single-free-face TTC test was carried out on Beishan granite. During that test, the failure process of the specimen was monitored by a high-speed camera. The failure forms of the specimens under the three loading conditions were different, especially for the model test under biaxial compression and the single-free-face TTC test. Although the specimen failed due to compressive stress concentration under the latter two loading conditions, the failure form of the specimen was spalling in the model test and strain burst in the TTC test. The reason for this difference in failure was analysed (see the Discussion section) to better understand the triggering conditions and mechanisms of strain burst.

Specimens and experimental procedures

Specimens

The tested granite specimens in the present study were taken from the Beishan area of Gansu Province in China. This area has been preliminarily determined to be the preferred candidate site for China's high-level radioactive nuclear waste (HLW) repository. The properties of the Beishan granite are presented in Table 1. Regarding the specimen size of the model test, this study comprehensively considered factors such as the loading capacity of the loading system, boundary effects, and size effects and referred to rock model tests carried out by other scholars (e.g., He et al. 2012; Gong et al. 2018; Hu et al. 2019). The rock model specimens were prismatic with a size of 300 mm × 300 mm × 67 mm and a central hole 57 mm in diameter, as shown in Fig. 2a. This size ensures that the lateral dimensions of the rock specimen are greater than 5 times the diameter of the hole, weakening the boundary effect. For single-free-face TTC testing, the specimen was prismatic with dimensions of 100 mm × 100 mm × 200 mm, which meets the requirements of an approximate width: length ratio of 1:2, as suggested by ISRM (Feng et al. 2019), as shown in Fig. 2b.

Experimental apparatus

The model tests were carried out on a ZJCS-5000 biaxial loading apparatus, as shown in Fig. 3a (Peng et al. 2019). The load capacity of the apparatus is 5000 kN both vertically and horizontally. A DIC system was used in the model tests to monitor the full-field strains at the front surface of the specimens. The DIC system includes two digital cameras, an LED light source, a Vic-Snap image

Table 1 Basic mechanical properties and mineral contents of Beishan granite

UCS (MPa)	Young's modulus (GPa)	Poisson's ratio	Mineral content (%)			
			Feldspar	Quartz	Clay	Others
140	47.2	0.28	57.0	33.0	2.0	8

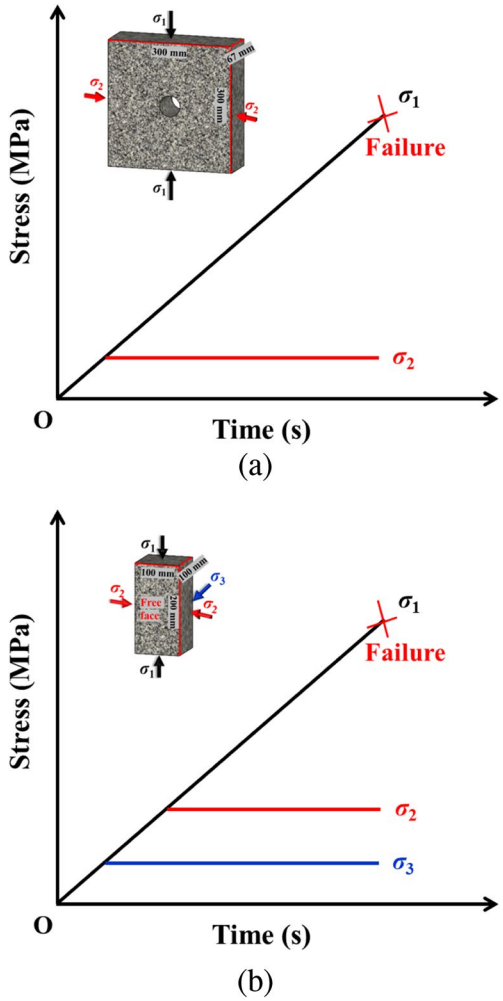

Fig. 2 Schematic diagram of the loading path and stress state of specimens in a model test (**a**) and a single-free-face TTC test (**b**)

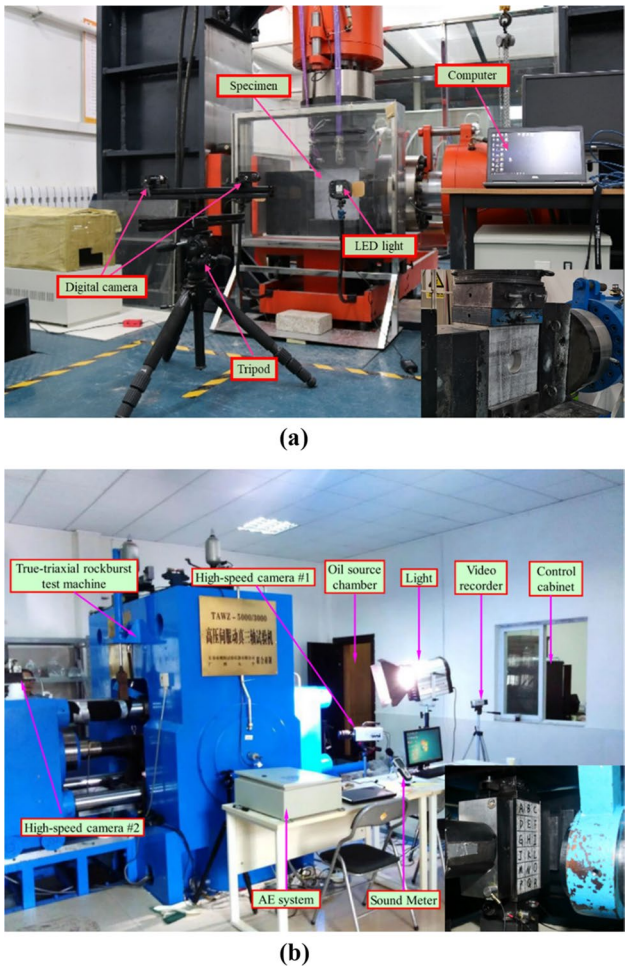

Fig. 3 **a** The biaxial loading apparatus ZJC-5000. **b** The novel true triaxial rock burst test apparatus (Su et al. 2017a)

acquisition system, and a digital processing system. Furthermore, a video camera monitored the failure process of the hole during testing.

The single-free-face TTC test was conducted on a novel true triaxial rock burst test apparatus (see Fig. 3b), which has a stiffness of 9 GN/m in the vertical direction and a stiffness of 5 GN/m in the horizontal direction. The axial and lateral load capacities of the machine are 5000 kN and 3500 kN, respectively. Loads can be applied to the specimen in three orthogonal directions. In this test, the failure process of the specimen was monitored by a high-speed camera.

Experimental procedures

Regarding the model tests, the loading path and stress state of a rock specimen are shown in Fig. 2a. σ_2 was 0 MPa and 5 MPa for the uniaxial and biaxial loading conditions, respectively. The loading process was divided into two stages. σ_2 was first increased to a predetermined value at a loading rate of 300 N/s under load control. Then, σ_2 was kept constant, and σ_1 was applied at a loading rate of 0.04 mm/s under displacement control until rock failure occurred. The criteria for rock failure here were severe splitting of the model specimen or through-type failure from the hole. This is because continued loading of the specimen in these two states may result in collapse, which is not conducive to analysis of its failure mode after the test.

For the single-free-face TTC test, the loading path and stress state of a rock specimen are shown in Fig. 2b. The loading process of this test was divided into three stages. First, σ_1, σ_2, and σ_3 were synchronously increased to 5 MPa. Then, σ_1 and σ_2 were simultaneously increased to 30 MPa, while σ_3 remained unchanged. Finally, σ_1 was increased until failure of the specimen, while both σ_2 and σ_3 remained unchanged. The stresses were applied at a rate of 0.5 MPa/s in all three stages.

Experimental results

Model test

Failure modes

Figure 4 shows an overview of the back side of the Beishan granite specimen after uniaxial and biaxial compression testing. The uniaxial and biaxial compression tests were terminated at σ_1 = 66.8 MPa and σ_1 = 120 MPa, respectively. Under uniaxial compression, the specimen formed four tensile fractures, with the longest and shortest fractures having lengths of 155 mm and 31 mm, respectively, as shown in Fig. 4a. In addition, the sidewalls of the hole under uniaxial compression did not produce breakout notches. Under biaxial compression, breakout notches were formed in the sidewalls of the hole to depths of 5.86–11.71 mm within the surrounding rock, as shown in Fig. 4b. It is obvious that the lateral stress changes the specimen failure mode from failure by tensile fracture formation to breakout notch failure of the sidewalls.

Failure process

Figure 5 shows the fracturing moments at a few stress levels during testing under uniaxial compression. The first fracture was initiated in the floor of the hole when σ_1 = 64.2 MPa, as shown in Fig. 5a. The fracture gradually propagated as σ_1 increased. Then, a macro fracture suddenly appeared on one sidewall of the hole and extended downwards when σ_1 was slightly increased to 64.4 MPa (Fig. 5b). Afterwards, a further increase of 0.3 MPa in σ_1 resulted in a fracture in the middle of the roof of the hole (Fig. 5c). A long fracture appeared on the other sidewall of the hole but propagated

Fig. 4 Overview of the back side of the Beishan granite specimen after testing under uniaxial (**a**) and biaxial compression (**b**)

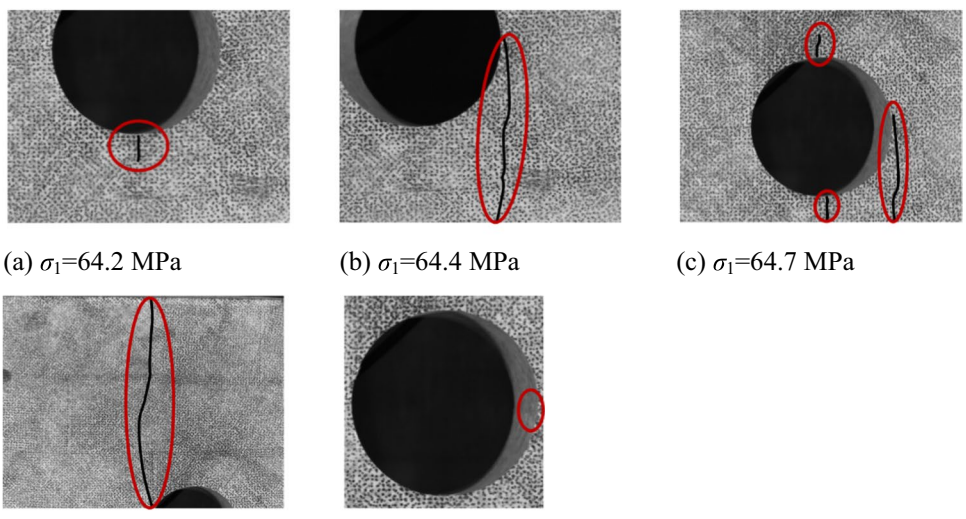

Fig. 5 Video images of the front side of the Beishan granite specimen showing the fracturing process under uniaxial compression

upwards when σ_1 was increased to 65.2 MPa (Fig. 5d). Slight pop-up spalling occurred on one sidewall of the hole when the test was terminated at 66.8 MPa (Fig. 5e). This failure process shows that the other tensile fractures formed in a very short time after the first tensile fracture event and that the most predominant tensile fractures formed in the sidewalls of the hole rather than in the roof and floor.

Figure 6 shows the fracturing moments at a few stress levels during testing under biaxial compression. The first pop-up spalling occurred on the right sidewall of the hole when σ_1 was 88.4 MPa (Fig. 6a). At σ_1 = 96.7 MPa, pop-up spalling also appeared on the left sidewall, and obvious spalling appeared on the right sidewall (Fig. 6b). Afterwards, spalling extended through the entire depth of the specimen, and breakout notches gradually formed in the sidewalls as σ_1 increased (Fig. 6c, d). The test was terminated at σ_1 = 116.7 MPa, with some small debris having spalled from the sidewalls and accumulated on the floor of the hole. This failure process shows that the model specimen under biaxial compression failed by spalling, which was a progressive formation.

Full-field strain development process

Figure 7 shows the full-field strain cloud images of the DIC in the Beishan granite specimen under uniaxial compression.

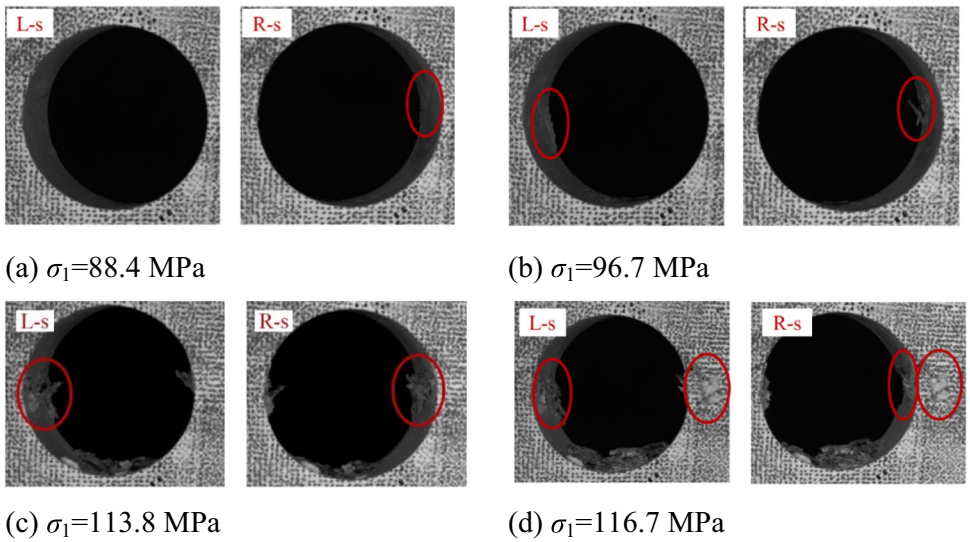

Fig. 6 Video images of the front side of the Beishan granite specimen showing the fracturing process under biaxial compression for σ_2 = 5 MPa

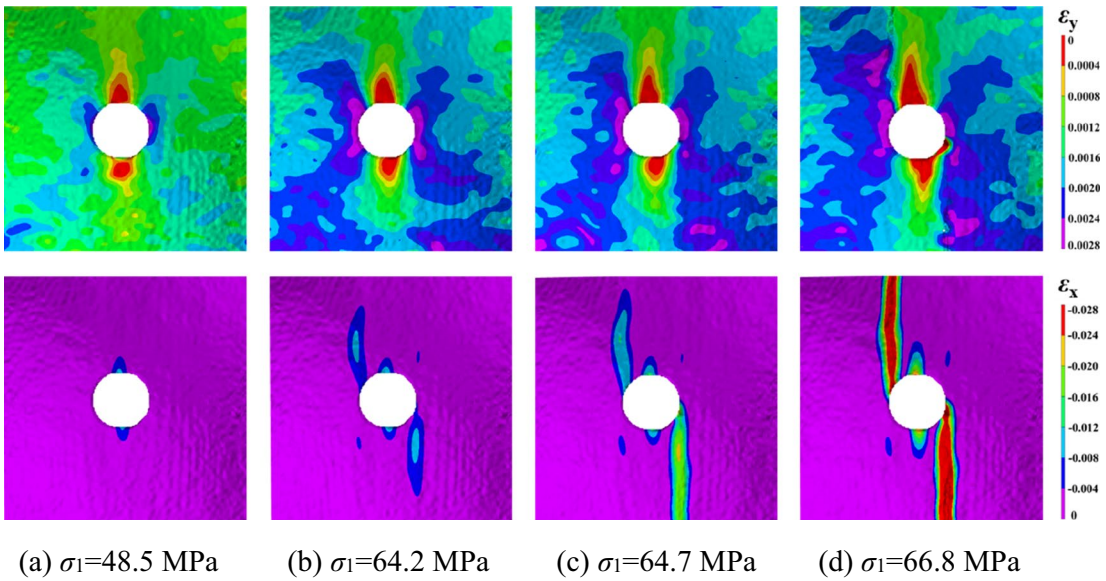

Fig. 7 DIC images of the front side of the Beishan granite specimen showing the evolution of the principal strains ε_y and ε_x under uniaxial compression; "+" indicates compressive strain, and "−" indicates tensile strain

The orientations of the principal strains ε_y and ε_x were vertical and lateral, respectively. Figure 7 shows that the tensile fractures in the specimen were associated with ε_x. The ε_x concentrations first appeared in the middle of both the roof and the floor in the early stage of loading, as shown in Fig. 7a. At $\sigma_1 = 64.2$ MPa, that is, when the first tensile fracture occurred in the specimen (Fig. 5a), the tensile strains ranged from −0.008 to −0.012 based on the DIC image of ε_x, as shown in Fig. 7b. Therefore, the range of −0.008 to −0.012 may be the critical strain interval for tensile fractures in the Beishan granite. The DIC image shows that similar strains appeared in the roof, upper left shoulder, and lower right haunch of the hole (Fig. 7b). At $\sigma_1 = 64.7$ MPa, all ε_x concentration areas were enlarged, with significant elevations in the lower right haunch, where the strains dominated in the range from −0.012 to −0.024, as shown in Fig. 7c. At this stress level, a long tensile fracture was created, and a roof fracture became visible (Fig. 5c). A fracture in the upper left shoulder suddenly became visible and extended to a length of approximately 44 mm when σ_1 was slightly increased by 0.3 to 61.5 MPa, as shown in Fig. 5d. At $\sigma_1 = 66.8$ MPa, ε_x increased from −0.024 to −0.028 in the positions of the tensile fractures (Fig. 7d), indicating further fracture propagation.

Figure 8 shows the full-field strain cloud images of the DIC in the Beishan granite specimen under biaxial compression. The spalling and breakout processes in the sidewall of the hole were reflected by the changes in ε_y during testing. At $\sigma_1 = 88.4$ MPa, the first pop-up spalling occurred on the right sidewall of the hole, and ε_y ranged from 0.0034 to 0.0039 in the sidewalls (Fig. 8a). At $\sigma_1 = 96.7$ MPa, the spalling zones of $\varepsilon_y = 0.0034$ to 0.0039 expanded in the walls, and dark clouds of falling debris also appeared on the wall surfaces (Fig. 8b). At $\sigma_1 = 113.8$ MPa, the spalling zone in the right sidewall became irregular, and the dark clouds extended deeper into the sidewalls, indicating that a good amount of debris had fallen and that breakout notches were being formed in the sidewalls, as shown in Figs. 6c and 8c. At $\sigma_1 = 116.7$ MPa, the spalling zones spread from the walls to the depths, but the immediate sidewall areas had lower ε_y values (Fig. 8). The relief in ε_y was a consequence of the unloading after the crushed material in the notches fell.

Comparing the DIC cloud images of ε_x in Fig. 8 with the evolution of the spalling in the sidewalls shown in Fig. 6, ε_x at spalling onset was in the range from −0.009 to −0.011, which is similar to the tensile fracture onset strain observed under uniaxial compression. The spalling zone defined by $\varepsilon_x = -0.009$ to −0.011 expanded with an increase in the applied stress σ_1. Fig. 8 shows that relatively high ε_x values occurred in four zones in the shoulders and haunches of the hole in the DIC cloud images of ε_x, but the ε_x value was less than the critical strain value for spalling and splitting fracture onset. Thus, no tensile fractures were visible in the video images when the test was terminated at $\sigma_1 = 116.7$ MPa.

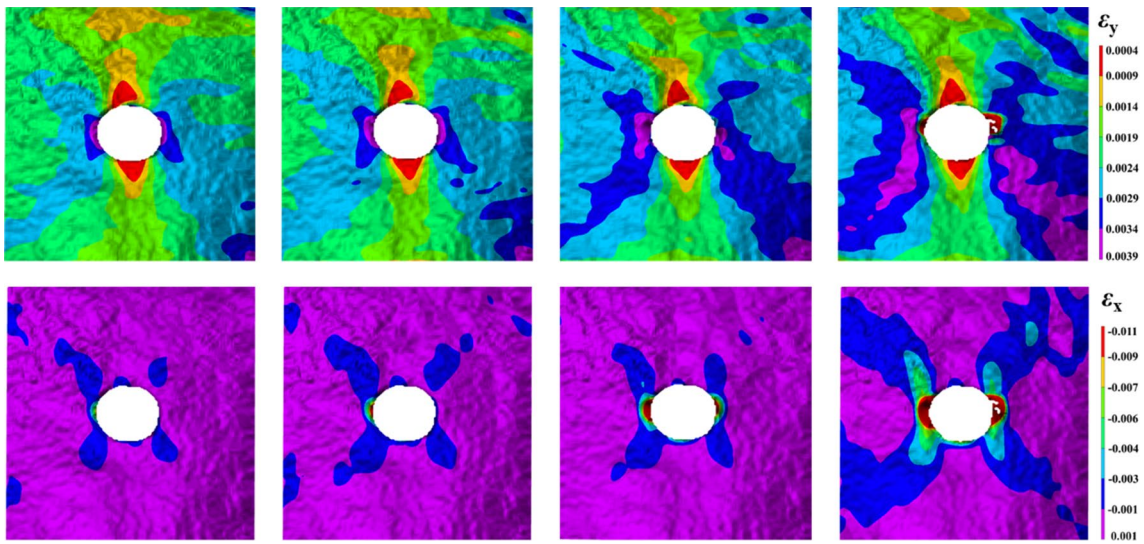

Fig. 8 DIC images of the front side of the Beishan granite specimen showing the evolution of the principal strains ε_y and ε_x under biaxial compression for $\sigma_2 = 5$ MPa

Single-free-face TTC test

Failure mode

Figure 9a shows the failure mode of a Beishan granite specimen after testing in the single-free-face TTC test. The free surface of the specimen in the σ_3 direction burst and collapsed, and fractures formed perpendicular to the σ_1–σ_3 plane. The fractures close to the free surface of the specimen were subparallel to the free surface and extensional, while the internal fractures were shear fractures.

Failure process

Figure 9b shows the typical failure process on the free surface recorded by a high-speed camera in a single-free-face TTC test. Some small rock particles were ejected from the upper region of the Beishan granite after σ_1 was loaded to approximately 95% of the peak stress of the tested specimen. After an approximately 0.53 s delay, a splitting fracture formed in the upper region of the specimen, and then the split rock plates were ejected away from the host rock. Afterwards, many rock fragments were ejected from the free surface and accompanied by a loud sound. Finally, a burst pit was formed on the free surface of the specimen. Obviously, the Beishan granite failed by strain bursting in the single-free-face TTC test. This failure form was significantly different from the compressive stress-induced sidewall failure behaviour of the model specimen under biaxial loading. The triggering condition of the strain bursts under the two loading modes is further analysed in the following section.

Discussion

Splitting fracture

Under uniaxial compression, the model specimen formed tensile fractures in the surrounding rock of the hole, especially at the top and bottom of the hole. These test results are helpful for interpreting fractures observed in some mountain tunnels. Figure 10a shows a short road tunnel subjected to a splitting fracture in the roof. The tunnel has a rock cover of less than 20 m and is less than 10 m from the mountain slope. The slope declines towards Trondheim Fjord, which extends 100 m below the left side of the tunnel. The lateral *in situ* stresses in the position of the tunnel are nearly zero because they are only a short distance from the slope. Therefore, the tangential stresses in the tunnel roof are tensile, even though their magnitudes are very low. Because of the tensile stresses, a geological discontinuity exposed on the ceiling of the southern entrance of the tunnel has opened several centimetres. Longitudinal splitting fractures appear on the roof along the entire tunnel length of 70 m. Some of the splitting fractures are marked by white lines in Fig. 10b, which shows the inside of the tunnel towards the northern exit. The rock types of the tunnel are gneiss and greenstone. The foliations in the rock mass are sub perpendicular to the tunnel length. Obviously, these splitting fractures are created by the tensile tangential stresses in the roof. Such splitting matches the tensile fracture pattern in the roof and floor of the hole in a Beishan granite specimen tested under uniaxial compression. The tensile fractures in the shoulders and floor corners of the hole in the specimen demonstrate that similar extensional fractures may exist in the rock mass surrounding tunnels

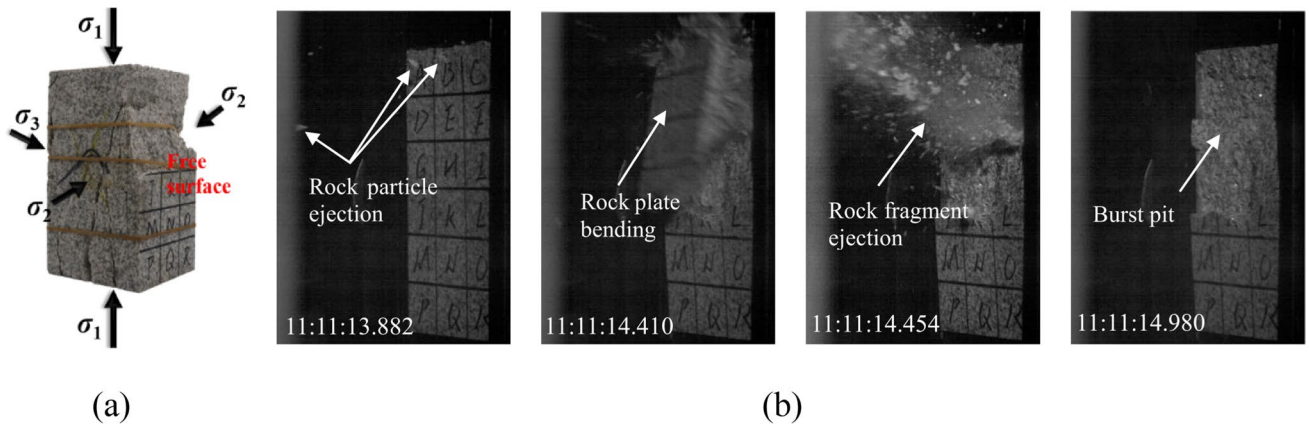

Fig. 9 Failure mode (**a**) (Shi et al. 2023b) and typical failure process (**b**) of a Beishan granite specimen in a single-free-face TTC test

(a)

(b)

Fig. 10 A road tunnel near Trondheim fjord: a splitting fracture in the roof (**a**) and the details of the splitting fractures (**b**) (marked by the white arrows) along the length of the tunnel (photograph by Charlie C. Li)

close to mountain slopes where the lateral in situ stresses are approximately zero. To avoid such extensional fracturing, tunnels should be placed far from mountain slopes. A low horizontal in *situ-stress* could easily suppress tensile and extensional fracturing in and around the tunnel.

Progressive rock failure in a model test under biaxial compression

The lateral stress changes the model specimen failure from splitting failure to breakout notch failure in the sidewalls. Under biaxial compression, Beishan granite specimen failure starts with spalling and ends with the formation of breakout notches. The breakout notches of the Beishan granite are similar to the V-shaped notches formed in the Mine-by Experiment tunnel of the AECL underground laboratory, as shown in Fig. 11 (Read 2004).

The spalling onset stress and the breakout notch depth are two important parameters that describe breakout rock failure. Martin et al. (1999) proposed the following relationship between the notch depth and the maximum tangential stress ($\sigma_{\theta\max}$) value in the tunnel wall based on field observations:

$$\frac{R_f}{a} = 0.49(\pm 0.1) + 1.25\frac{\sigma_{\theta\,\max}}{\sigma_c} \quad (1)$$

where R_f is the distance from the notch tip to the tunnel centre; a is the tunnel radius; $\sigma_{\theta\max}$ is the maximum tangential stress, which is estimated by the Kirsch solution $\sigma_{\theta\max} = 3\sigma_1 - \sigma_2$ for circular tunnels; and σ_c is the uniaxial compressive strength of the rock.

Using the Kirsch solution, $\sigma_{\theta\max}$ of the sidewalls of the Beishan granite specimen under biaxial compression is 260 MPa. The magnitude of $\sigma_{\theta\max}/\sigma_c$ at the onset of spalling is 1.8, approximately 3.7 times the spalling onset stress (0.49 ± 0.1) obtained from Eq. (1). This discrepancy has also been observed in similar laboratory model tests by Gong et al. (2018) and Hu et al. (2019) (Fig. 12). In response to this problem, some scholars have shown that the curvature of the hole affects the onset of spalling and have tested specimens with different hole diameters. The magnitudes of $\sigma_{\theta\max}/\sigma_c$ at the onset of spalling in those tests were greater than 1 and decreased with the hole diameter, as shown in Fig. 12, confirming that the curvature of the hole significantly affects the spalling onset stress in laboratory tests. The curvature of the small holes used in laboratory tests is less than one-hundredth of the curvature of tunnels. A smaller curvature possibly results in confinement to the material around the hole such that a higher tangential stress is needed to initiate spalling, which may be the mechanical mechanism for the increase in the spalling onset stress in laboratory tests. Therefore, the empirical Eq. (1) obtained based on on-site observations is not suitable for determining the fracture initiation stress in laboratory-based small-scale model specimens.

Strain energy stored in the rock surrounding a circular hole

To understand the fracture range of the model specimen, the strain energy concentration characteristics of the rock surrounding the hole are further analysed. Here, the

(a) (b)

Fig. 11 Mine-by Experiment tunnel photographs showing the final shape of V-shaped breakout notches in the crown and invert of the tunnel (**a**) and a close-up of notch tips at the tunnel invert (**b**) (Read 2004)

Beishan granite is assumed to be a continuous linear elastic rock. If the specimen does not contain a circular hole, its elastic strain energy density V_0 can be expressed as follows (He et al. 2016):

$$V_0 = \frac{1+\nu}{2E}\left[(1-\nu)\left(\sigma_1+\sigma_2\right)^2 - 2\sigma_1\sigma_2\right] \tag{2}$$

where E and ν are Young's modulus and Poisson's ratio, respectively.

Therefore, for a specimen without a circular hole, the elastic strain energy W_0 stored in the annulus between b and a can be expressed as follows:

$$W_0 = \pi\left(b^2 - a^2\right)hV_0 \tag{3}$$

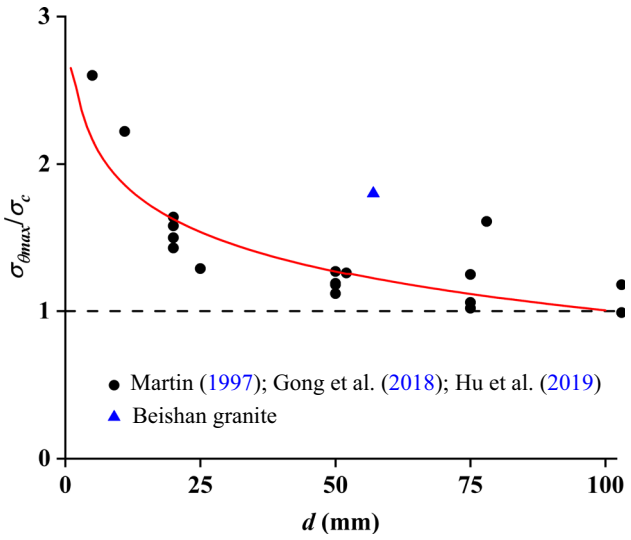

Fig. 12 Relationship between the maximum tangential stress at the onset of spalling and the hole diameter (Martin 1997; Gong et al. 2018; Hu et al. 2019)

where a is the radius of the hole (28.5 mm here) and b is the distance from the considered position to the centre of the specimen. h stands for the thickness of the model specimen and is 67 mm.

In fact, the model specimen contains a circular hole, so the elastic strain energy W_e stored in the annulus between b and a during loading can be expressed as follows (He et al. 2016):

$$W_e = \frac{\pi h}{E}\left\{\begin{array}{c}(1-\nu^2)\int_a^b\left[\left(\sigma_1+\sigma_2\right)^2 r + 2\left(\sigma_1-\sigma_2\right)^2\frac{a^4}{r^3}\right]dr + \\ 2(1+\nu)\int_a^b\left[\frac{\left(\sigma_1+\sigma_2\right)^2}{4}\frac{a^4}{r^3} + \frac{\left(\sigma_1-\sigma_2\right)^2 a^4}{4}\left(\frac{2}{r^3} - \frac{12a^2}{r^5} + \frac{9a^4}{r^7}\right) - \sigma_1\sigma_2 r\right]dr\end{array}\right\} \tag{4}$$

The strain energy storage coefficient k_e expresses the degree of strain energy concentration in the surrounding rocks induced by a circular hole:

$$k_e = \frac{W_e - W_o}{W_o} \times 100 \tag{5}$$

According to Eqs. (2)–(5), W_e, W_0, and k_e are calculated at different b values, and the calculation results are presented in Table 2. Notably, σ_1 is the fracture onset stress of the surrounding rock of the hole. Under both the uniaxial and biaxial loading conditions, the W_e and W_o values of the Beishan granite increased as b increased, and k_e decreased as b increased. As shown in Fig. 13, the strain energy characteristics of the Beishan granite under biaxial compression showed that k_e was 67.5% at $b = 1.5a$, 41.6% at $b = 2a$, 20.1% at $b = 3a$, 11.9% at $b = 4a$, and 7.7% at $b = 5a$, indicating a greater strain energy concentration in the surrounding rock in the range of $1.5a$. This strain energy concentration feature is also valid for the Beishan granite under uniaxial compression (k_e is 64.8% at $b = 1.5a$), as shown in Table 2. In addition, the "Failure modes" section shows that the maximum depth of the surrounding rock notch is

Table 2 Summary of the strain energy of the surrounding rocks at different b values in the model tests

b (mm)	W_0 (J)		W_e (J)		k_e (%)	
	UCT	BCT	UCT	BCT	UCT	BCT
43	8.8	16	14.5	26.8	64.8	67.5
57	20.6	37.5	28.9	53.1	40.3	41.6
86	55.8	101	66.8	121.8	19.7	20.1
114	103.2	187.7	115.3	210	11.7	11.9
143	166.3	302.5	179	325.8	7.6	7.7

When calculating the strain energy, σ_1 was 64.4 MPa and 88.4 MPa under uniaxial and biaxial compression, respectively

UCT uniaxial compression test, *BCT* biaxial compression test

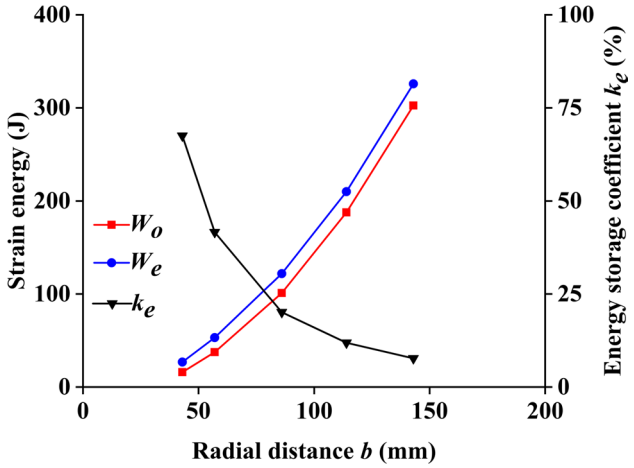

Fig. 13 Strain energy characteristics of the surrounding rock at different depths for a Beishan granite specimen under biaxial compression: σ_1 was 88.4 MPa

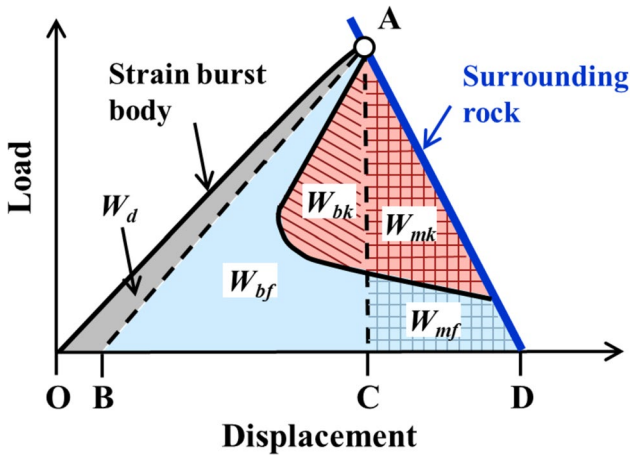

Fig. 14 A conceptual model for the energy conversions during a strain burst event: the strain energy stored in the strain burst body is $W_b = (W_{bf} + W_{bk})$, and the strain energy released from the surrounding rock mass is $W_m = (W_{mf} + W_{mk})$ (Li et al. 2022)

approximately 1.2a, which is consistent with the strain energy concentration range.

Difference between the model test failure and single-free-face TTC test failure

The test results showed that the failure forms of the Beishan granite specimens in the model test with biaxial stresses were different from those in the single-free-face TTC test. Under a high compressive stress (i.e., in the surrounding rock elements perpendicular to σ_1 in the model test), the sidewalls of the model specimen failed by spalling, that is, static failure. However, in the single-free-face TTC test, the Beishan granite acted as a sidewall element, and it failed via strain bursting, showing dynamic failure characteristics. In this section, from the perspective of the strain burst kinetic energy source, the reasons for the difference in the failure forms of the Beishan granite specimens under the above two loading methods are discussed.

Strain burst will occur when the total strain energy stored in the rock isto be ejected and the energy released from the surrounding rock is greater than the energy needed for rock fracturing. In other words, there is excess energy in the rock that is converted into kinetic energy to eject the rock. Li et al. (2022) proposed a conceptual model to analyse the source of kinetic energy in a strain burst event, as shown in Fig. 14. In Fig. 14, line OA represents the pre-peak behaviour of the strain burst body. When the burst body is loaded to the peak load point A, a small amount of energy is used to generate microcracks, that is, the dissipated energy W_d in Fig. 13. The rest is stored in the strain burst body, that is, the elastic energy $W_b = (W_{bf} + W_{bk})$. Among them, W_{bf} is used to fracture the strain burst body at the post-peak stage, and W_{bk} is converted into kinetic energy to eject the rock. The above-mentioned W_d, W_{bf}, and W_{bk} describe the transformation of the strain energy stored by the strain burst body. In

addition, in this conceptual model, the blue line AD represents the response of the surrounding rock during a strain burst, and its slope represents the overall stiffness of the surrounding rock. The strain energy released from the surrounding rock is denoted as $W_m = (W_{mf} + W_{mk})$, where W_{mf} is the portion dissipated by rock fracture and W_{mk} is the portion converted into kinetic energy. In summary, the kinetic energy W_k of the strain burst comes from the W_{bk} stored in the strain burst itself and the W_{mk} provided by the surrounding rock.

For the model specimen, the sidewall rock of the circular hole can be considered a potential strain burst body. The kinetic energy contributed by the potential strain burst body itself, W_{bk}, depends on the rock type and is a constant per unit volume for a given lithology (Tarasov and Potvin 2012; Zhang and Li 2019; Shi et al. 2023a). It can therefore be defined as the intrinsic potential energy of strain bursts and can be obtained from the uniaxial compressive stress–strain curve of the rock under servo control. The W_{bk} value is 1.5 kJ/m^3 for the Beishan granite (Shi et al. 2023a), which is much smaller than the value for the Kuru granite of 28.3 kJ/m^3 calculated by Zhang and Li (2019), indicating that the W_{bk} value of the Beishan granite is very small.

In addition, the "Progressive rock failure in a model test under biaxial compression" section shows that the failure onset stress of the potential strain burst body was much higher than its uniaxial compressive strength due to the influence of the curvature and structure of the circular hole. This means that the failure of the potential strain burst body in the model test required more fracture energy. Therefore, in the model test, the strain energy accumulated in the potential strain burst body of Beishan granite was mainly used for its fracturing.

For a rock with low W_{bk}, the key factor for triggering a strain burst in the model test is the magnitude of W_{mk} provided by the surrounding rock. W_{mk} is negatively related to the radial stiffness (K_{rb}) of the surrounding rock mass. In other words, the smaller the K_{rb} value of the surrounding rock mass is, the greater the W_{mk} provided to the strain burst body. For a circular tunnel, the K_{rb} value of the surrounding rock mass can be expressed as follows (Zhao et al. 2021):

$$K_{rb} = \frac{E}{1+\nu}\frac{1}{b} \tag{6}$$

where $E = 47.2$ GPa and $\nu = 0.28$ are Young's modulus and Poisson's ratio of the rock, respectively, and b is the distance from the considered position to the tunnel centre.

Because the distance from the notch tip to the specimen centre was 40.21 mm, b in Eq. (6) was set to 45 mm in this study. K_{rb}, calculated using Eq. (6), was 819 GPa/m for the Beishan granite, indicating that the K_{rb} of the surrounding rock mass was higher. Therefore, the Beishan granite had low W_{bk} and high surrounding rock stiffness, and neither the potential strain burst body nor the surrounding rock mass could provide sufficient kinetic energy to induce a strain burst.

Previous studies have shown that some model specimens failed by strain bursting under multiaxial stress conditions. For example, Hu et al. (2019) carried out a similar model test on a Guangdong granite specimen with a circular hole, where the specimen was also subjected to biaxial compression with $\sigma_2 = 5$ MPa. The Guangdong granite specimen

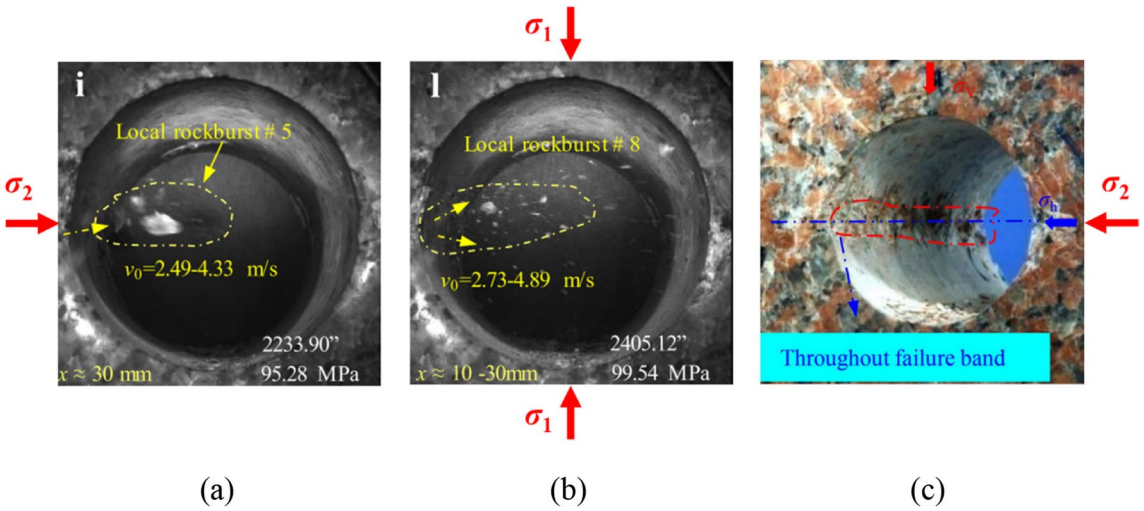

Fig. 15 Strain burst failure of a Guangdong granite specimen under biaxial compression with σ_2=5 MPa: Images of strain bursts at σ_1 = 95.28 MPa (**a**) and σ_1 = 99.54 MPa (**b**) recorded by a high-speed camera and failure notches in one sidewall of the hole in the Guangdong granite specimen (**c**) (Hu et al. 2019)

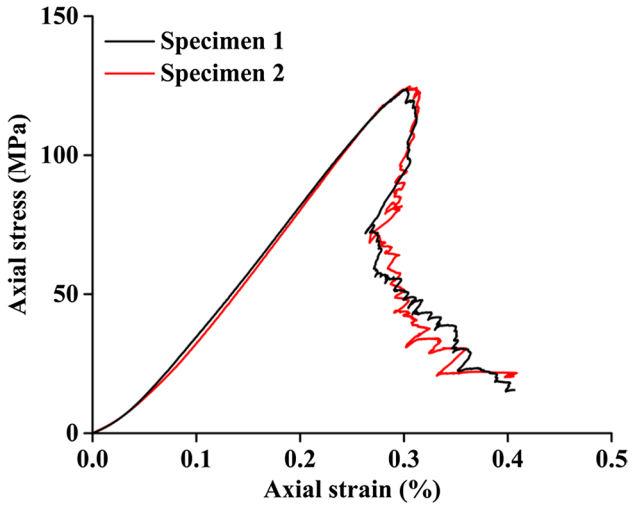

Fig. 16 Axial stress–strain curves of cylindrical specimens of Guangdong granite under uniaxial compression

experienced strain bursts during loading (see Fig. 15a, b), and breakouts formed in the sidewalls of the hole (see Fig. 15c). According to the stress–strain curve of cylindrical specimens of Guangdong granite tested under uniaxial compression (Fig. 16), its $W_{bk} = 12$ kJ/m^3 is 8 times that of Beishan granite. This means that when model tests are carried out on the Guangdong granite specimen, a large portion of the accumulated strain energy in the potential strain burst body is transformed into kinetic energy to eject the rock.

In the single-free-face TTC test, the Beishan granite specimen simulates the stress state of a rock element on the sidewall of the tunnel, which can be called a potential strain burst body. The true triaxial test system can be regarded as the surrounding rock. The vertical and horizontal stiffnesses of the loading system used are 9 GN/m and 5 GN/m, respectively, which are greater than the 5 GN/m proposed by ISRM (Fairhurst and Hudson 1999) and correspond to a high-stiffness test apparatus. Therefore, the influence of its deformation energy on the failure of the specimen does not need to be considered. In other words, the influence of the surrounding rock can be ignored when discussing rock failure here. In this case, as long as σ_1 exceeds the bearing capacity of the rock specimen and there is excess strain energy, i.e., W_{bk}, a strain burst can be triggered.

Engineering application

Three types of laboratory tests were conducted in the present study, and the failure forms presented by these three tests correspond to splitting, spalling, and strain burst in hard rock engineering, as shown in Table 3. Rock splitting is mainly induced by tensile stress concentration and is prone to occur in hard rock engineering without lateral stress constraints, such as in the case of the road tunnel shown in Fig. 10. To avoid such splitting failures, such a tunnel should be excavated in the rock mass with horizontal stress constraints. Rock spalling and strain burst are two very similar forms of failure, both of which are induced by compressive stress concentrations. The main difference between the two is whether the fractured rock can be ejected: if it can, a strain burst occurs; if not, spalling occurs. The analysis of the "Difference between the model test failure and single-free-face TTC test failure" section shows that the kinetic energy of rock ejection in the rock model test mainly comes from the burst rock, that is, the W_{bk} shown in Fig. 14. This conclusion also applies to strain burst events that occur at deep hard rock engineering sites. The typical feature of a strain burst is the small volume of the burst pit, which means that the deformation of the surrounding rock of the burst rock is relatively small. Li et al. (2022) used numerical simulation to quantitatively evaluate the effect of bust pit depth on the magnitude of kinetic energy supplied by the surrounding rock and the burst body and showed that for shallower burst pits, the kinetic energy is mainly supplied by the burst rock. Therefore, the intensity of strain bursts can be preliminarily evaluated by the intrinsic potential

Table 3 Summary of test types and corresponding test results

Test type	Model testing			Single-free-face TTC testing
Rock type	Beishan granite	Beishan granite	Guangdong granite (Hu et al. 2019)	Beishan granite
Stress state	Uniaxial stress	Biaxial stress	Biaxial stress	True triaxial stress
Stress levels	$\sigma_3 = 0$, $\sigma_2 = 0$, $\sigma_1 = 66.8$ MPa	$\sigma_3 = 0$, $\sigma_2 = 5$ MPa, $\sigma_1 = 120$ MPa	$\sigma_3 = 0$, $\sigma_2 = 5$ MPa, $\sigma_1 = 99.54$ MPa	$\sigma_3 = 5$, $\sigma_2 = 30$ MPa, $\sigma_1 = 248$ MPa
Failure mode	Tensile fractures were formed at the roof, floor, and sidewalls of a hole, the longest of which was 155 mm	Breakouts were formed in the sidewalls of the hole	Breakouts were formed in the sidewalls of a hole	Burst pits and shear fractures were formed on the free surface and inside of the specimen, respectively
Failure form	Splitting	Spalling	Strain burst	Strain burst

energy W_{bk} of the rock. For rocks with higher W_{bk}, such as Guangdong granite (Hu et al. 2019), the excavation of such rock masses is prone to triggering strain bursts, and it is suggested to consider dynamic support elements, such as yielding and energy-absorbing rock bolts, in the support system. For rocks with a low W_{bk}, such as Beishan granite, the excavation of such rocks is not prone to triggering spalling, and light dynamic support elements can be considered for the support system.

Conclusions

In the model test, the specimen under uniaxial loading was prone to tensile fractures, especially fractures in the shoulders and haunches of the hole, which extend remarkably and finally result in splitting of the specimen. The lateral stress transforms the tensile fractures of the specimen into breakouts in the areas where compressive stress is concentrated. The intrinsic potential energy (W_{bk}) of the rock determines how the breakout is formed. If the W_{bk} value of the rock is high, the breakout is formed by a strain burst, such as in the Guangdong granite. If the W_{bk} value of the rock is low, the breakout is formed by spalling, such as in the Beishan granite.

For the model specimens with a circular hole, the strain energy stored in the surrounding rock increases significantly, especially in the range of 1.5 times the radius. The strain energy storage coefficient of the surrounding rock at 1.5 times the radius is approximately 65%, indicating that the surrounding rock in this range is prone to fracturing.

In the single-free-face true triaxial compression testing, fractures perpendicular to the σ_1–σ_3 plane were observed in the Beishan granite specimen, slight strain bursts occurred on the free surface of the specimen, and a burst pit was formed. In this test, the triggering condition of strain bursts is that W_{bk} is greater than 0, and the specimens in this test were more prone to strain bursting than those in the model test.

Acknowledgements The authors thank Prof. Charlie C. Li at Norwegian University of Science and Technology for his improvements to the paper.

Funding It is acknowledged that the tests were financially supported by the National Key R&D Program of China under Grant No. 2018YFC0407006 and the 111 Project under Grant No. B17009.

Data availability All data are reported in the paper.

Declarations

Conflict of interest The authors declare are no competing interests.

References

Carter BJ (1992) Size and stress gradient effects on fracture around cavities. Rock Mech Rock Eng 25:167–186

Cheon DS, Jeon S, Park C, Song WK, Park ES (2011) Characterization of brittle failure using physical model experiments under polyaxial stress conditions. Int J Rock Mech Min Sci 48(1):152–160

Cook NGW (1963) The basic mechanics of rockbursts. J South Afr Inst Min Metall 64(3):71–81

Du K, Tao M, Li XB, Zhou J (2016) Experimental study of slabbing and rockburst induced by true-triaxial unloading and local dynamic disturbance. Rock Mech Rock Eng 49:3437–3453

Fairhurst C, Cook NGW (1966) The phenomenon of rock splitting parallel to the direction of maximum compression in the neighborhood of a surface. In: Proceedings of the 1st Congress of the International Society of Rock Mechanics. Lisbon, Portugal, pp 687–692

Fairhurst CE, Hudson JA (1999) Draft ISRM suggested method for the complete stress-strain curve for intact rock in uniaxial compression. Int J Rock Mech Min Sci 36(3):281–289

Fakhimi A, Carvalho F, Ishida T, Labuz JF (2002) Simulation of failure around a circular opening in rock. Int J Rock Mech Min Sci 39(4):507–515

Feng XT, Haimson B, Li XC, Chang CD, Ma XD, Zhang X, Ingraham M, Suzuki K (2019) ISRM suggested method: determining deformation and failure characteristics of rocks subjected to true triaxial compression. Rock Mech Rock Eng 52:2011–2020

Gong FQ, Luo Y, Li XB, Si XF, Tao M (2018) Experimental simulation investigation on rockburst induced by spalling failure in deep circular tunnels. Tunn Undergr Space Technol 81:413–427

Gong FQ, Luo Y, Liu DQ (2019) Simulation tests on spalling failure in deep straight-wall-top-arch tunnels. Chin J Geotech Eng 241:1091–1100

Gong FQ, Wu WX, Li TB (2020) Simulation test of spalling failure of surrounding rock in rectangular tunnels with different height-to-width ratios. Bull Eng Geol Environ 79:3207–3219

Haimson B, Chang C (2000) A new true triaxial cell for testing mechanical properties of rock, and its use to determine rock strength and deformability of Westerly granite. Int J Rock Mech Min Sci 37:285–296

Haimson B, Lee H (2004) Borehole breakouts and compaction bands in two high-porosity sandstones. Int J Rock Mech Min Sci 41:287–301

He BG, Zelig R, Hatzor YH, Feng XT (2016) Rockburst generation in discontinuous rock masses. Rock Mech Rock Eng 49:4103–4124

He M, Li J, Liu D, Lin K, Ren F (2021) A novel true triaxial apparatus for simulating strain bursts under high stress. Rock Mech Rock Eng 54:759–775

He M, Xia H, Jia X, Gong W, Zhao F, Liang K (2012) Studies on classification, criteria and control of rockbursts. J Rock Mech Geotech Eng 4(2):97–114

He MC, Zhao F, Cai M, Du S (2015) A novel experimental technique to simulate pillar burst in laboratory. Rock Mech Rock Eng 48:1833–1848

Hu XC, Su GS, Chen GY, Mei SM, Feng XT, Mei GX, Huang XH (2019) Experiment on rockburst process of borehole and its acoustic emission characteristics. Rock Mech Rock Eng 52:783–832

Jiang B, Gu S, Wang L, Zhang G, Li W (2019) Strainburst process of marble in tunnel-excavation-induced stress path considering intermediate principal stress. J Central South Univ 26(4):984–999

Kusui A, Villaescusa E, Funatsu T (2016) Mechanical behaviour of scaled-down unsupported tunnel walls in hard rock under high stress. Tunn Undergr Space Technol 60:30–40

Li CC, Zhao TB, Zhang YB, Wan WK (2022) A study on the energy sources and the role of the surrounding rock mass in strain burst. Int J Rock Mech Min Sci 154:105114

Li X, Du K, Li D (2015) True triaxial strength and failure modes of cubic rock specimens with unloading the minor principal stress. Rock Mech Rock Eng 48:2185–2196

Lin H, Oh J, Canbula I, Stacey TR (2020) Experimental and analytical investigations of the effect of hole size on borehole breakout geometries for estimation of in situ stresses. Rock Mech Rock Eng 53:781–798

Lu J, Yin GZ, Zhang DM, Li X, Huang G, Gao H (2021) Mechanical properties and failure mode of sandstone specimen with a prefabricated borehole under true triaxial stress condition. Geomech Energy Environ 25:100207

Luo Y, Gong F, Liu D, Wang S, Si X (2019) Experimental simulation analysis of the process and failure characteristics of spalling in D-shaped tunnels under true-triaxial loading conditions. Tunn Undergr Space Technol 90:42–61

Martin CD (1997) Seventeenth Canadian geotechnical colloquium: the effect of cohesion loss and stress path on brittle rock strength. Can Geotech J 34(5):698–725

Martin CD, Kaiser PK, Mccreath DR (1999) Hoek-Brown parameters for predicting the depth of brittle failure around tunnels. Can Geotech J 36(1):136–151

Mogi K (1967) Effect of the intermediate principal stress on rock failure. J Geophys Res 72(20):5117–5131

Ohta Y, Aydan Ö (2010) The dynamic responses of geo-materials during fracturing and slippage. Rock Mech Rock Eng 43:727–740

Peng JY, Zhang FP, Yan GL, Qiu ZG, Dai XH (2019) Experimental study on rock-like materials fragmentation by electric explosion method under high stress condition. Powder Technol 356:750–758

Read RS (2004) 20 years of excavation response studies at AECL's Underground Research Laboratory. Int J Rock Mech Min Sci 41(8):1251–1275

Sagong M, Park D, Yoo J, Lee JS (2011) Experimental and numerical analyses of an opening in a jointed rock mass under biaxial compression. Int J Rock Mech Min Sci 48(7):1055–1067

Shi L, Li CC, Zhang X, Feng XT (2023a) Experimental verification of the intrinsic strainburst proneness of various rock types. Bull Eng Geol Environ 82(4):119

Shi L, Li CC, Zhang X, Feng XT, Wang G (2022) Strength characteristics of brittle rocks under multi-stage intermediate principal stress loading. Géotech Lett 12(2):101–105

Shi L, Zhang X, Sharifzadeh M, Qi Z, Li Y, Xu Q (2023b) Experimental study on the relationship between local deformation and macro-crack evolution of granite under conventional triaxial compression. Eur J of Environ and Civ Eng 27(5):2210–2227

Si X, Li X, Gong F, Huang L, Ma C (2022) Experimental investigation on rockburst process and characteristics of a circular opening in layered rock under three-dimensional stress conditions. Tunn Undergr Space Technol 127:104603

Si XF, Huang LQ, Gong FQ, Liu XL, Li XB (2020) Experimental investigation on influence of loading rate on rockburst in deep circular tunnel under true-triaxial stress condition. J Central South Univ 27(10):2914–2929

Su G, Feng X, Wang J, Jiang J, Hu L (2017a) Experimental study of remotely triggered rockburst induced by a tunnel axial dynamic disturbance under true-triaxial conditions. Rock Mech Rock Eng 50:2207–2226

Su GS, Hu LH, Feng XT (2018) True triaxial experimental study of rockbursts induced by ramp and cyclic dynamic disturbances. Rock Mech Rock Eng 51:1027–1045

Su GS, Jiang JQ, Zhai SB (2017b) Influence of tunnel axis stress on strainburst: an experimental study. Rock Mech Rock Eng 50:1551–1567

Tarasov BG, Potvin Y (2012) Absolute, relative and intrinsic rock brittleness at compression. Min Technol 121(4):218–225

Von Karman T (1911) Festigkeitsversuche unter allseitigem. Druck Zeitschr Ver Dentsch Ing 55:1749–1757

Wan W, Li CC (2022) Microscopic and acoustic interpretations of the physics of rock burst and the difference in fracturing patterns in class I and class II rocks. Rock Mech Rock Eng 55(11):6841–6862

Wang Y, He M, Liu D, Ling K, Reng F (2021) Experimental study on impact rockburst of surrounding rock in deep elliptical caverns. Chin J Rock Mech Eng 40(11):2214–2228

Zhang H, Li CC (2019) Effects of confining stress on the post-peak behaviour and fracture angle of Fauske marble and Iddefjord granite. Rock Mech Rock Eng 52:1377–1385

Zhang YB, Liang P, Yao XL, Sun L, Tian BZ, Liu XX (2020) Experimental study of energy and frequency characteristics of acoustic emissions induced from tensile and shear cracks in tunnel rockburst process. Eur J Environ Civ Eng 26(9):3961–3980

Zhao H, Liu C, Huang G, Yu B, Liu Y, Song Z (2020) Experimental investigation on rockburst process and failure characteristics in trapezoidal tunnel under different lateral stresses. Construction and Building Materials 259:119530

Zhao T, Zhang Y, Li CC (2021) Radial stiffness of rock bolt samples and required thickness of the steel tube in impact tests. Int J Rock Mech Min Sci 146:104886

Zhao XG, Cai M (2014) Influence of specimen height-to-width ratio on the strainburst characteristics of Tianhu granite under true-triaxial unloading conditions. Can Geotech J 52(7):890–902

Zhong Z, Deng R, Lv L, Fu X, Yu J (2018) Fracture mechanism of naturally cracked rock around an inverted U-shaped opening in a biaxial compression test. Int J Rock Mech Min Sci 103:242–253

Zhu Q, Li D, Han Z, Xiao P, Li B (2022) Failure characteristics of brittle rock containing two rectangular holes under uniaxial compression and coupled static-dynamic loads. Acta Geotech 17:131–152